

Article

Experimental Observations of Turbulent Events in the Surfzone

Francesca De Serio ^{1,2,*}  and Michele Mossa ^{1,2} ¹ Polytechnic University of Bari, DICATECh, 70125 Bari, Italy² CoNISMa, Inter University Consortium for Marine Sciences, 00196 Rome, Italy; michele.mossa@poliba.it

* Correspondence: francesca.deserio@poliba.it; Tel.: +39-080-5963557

Received: 6 September 2019; Accepted: 23 September 2019; Published: 24 September 2019



Abstract: In coastal dynamics, large-scale eddies transport and spread smaller turbulent vortices both towards the sea surface, thus contributing to the processes of air-water gas transfer, and towards the sea bottom, inducing sediment pick-up and resuspension. The mechanical role of the breaking-induced vortices to the redistribution of turbulence and turbulent kinetic energy is still unclear and needs a more thorough study, possibly supported by more measurements in this field. Based on this, the present paper aims to investigate the effects of experimental breaking waves in the surf zone. Two regular breaking waves, a spiller and a plunger, which propagate on a fixed slope, were generated in a laboratory channel and were examined shoreward to the breaker line. The measurements of their velocities in the cross-shore plane were assessed by means of a 2D Laser Doppler Anemometer. At the same time and location, elevation data were also acquired using a resistive wave gauge. Here, the principal characteristics are addressed in terms of turbulent intensities, turbulent kinetic energy, length scales and coherent motions. Our results could thus contribute to better define conceptual models used in typical engineering applications in coastal areas.

Keywords: surf zone; plunging breaker; spilling breaker; turbulence intensity; coherent events

1. Introduction

Vorticity and turbulence associated with breaking waves make the surf zone of special significance within near-shore dynamics and coastal sediment transport [1–6]. Despite the long-term investigations, they are still far from being completely elucidated. Many studies showed that the turbulent flow due to wave breaking is characterized by the formation of large-scale vortex structures which swirl around each other and feature a variety of shapes, named coherent structures [1,7–10]. They primarily control sediment movements and cross-shore morphodynamic evolution. Therefore, predicting near shore morphodynamics requires a thorough knowledge of their formation and spreading throughout the water column, as well as their interactions with bottom sediments. The identification of coherent structures, based on vorticity or other turbulent features, is difficult along with the description of intermittent events of turbulent nature. Many methods have been used, such as quadrant analysis, wavelets, and ensemble averaging to discriminate turbulent fluctuations from the ordered wave motion. However, a thorough knowledge of the formation and spreading of these coherent structures in the surf zone is expected to better explain their interactions with bottom sediments and their effects on a tracers' diffusion [7].

Previous studies of the mechanism controlling the formation and evolution of coherent structures under breaking waves have mainly focused on spilling waves in analogy with bores and jumps, where they were first documented [11,12]. Only a few experimental studies examined this behavior under plunging waves [13,14], where stronger turbulence was observed due to the presence of the overturning jet and the splash-up cycle. Depending on the type of breaker, different types of large-scale

coherent vortices can be found in breaking waves [10]. Under a turbulent bore propagating as a spilling wave, Nadaoka et al. [15] first observed large dominant horizontal eddies present in the bore front, while behind the wave crest the flow structure changed rapidly into obliquely downward stretched (i.e., descending) eddies which are responsible for mass flux, and enhancing momentum transport [12]. In a laboratory study of spilling regular waves, Kubo and Sunamura [16] observed, along with obliquely descending vortices, a new type of large-scale turbulence which they called downburst. It is an aerated water mass descending without a great deal of rotation [7], diverging at the bed and producing more sediment movement than the obliquely descending vortices. The counter rotating vortices were also noted in experiments on spilling breaking by Ting and Nelson [17].

Using a large eddy simulation, Christensen and Deigaard [18] and Watanabe et al. [19] have both predicted the formation of counter-rotating vortices extending obliquely downward in plunging and weakly plunging regular waves. Ting and Reintz [20] observed in experiments on plunging waves the existence of a vortex loop with counter-rotating vorticity generated by the breaking-wave. LeClaire and Ting [21] experienced, in a laboratory, that that large eddies impinging on the bottom was the primary mechanism that lifted the sediment particles into suspension in the plunging case. Further, Ting and Beck [22] with their experiments, and Zou et al. [23] with numerical runs, found that for a plunging wave, the dominant sediment suspension mechanism was the outward and upward deflected flow field which originated by the splashing jet impinging at the bottom.

Ting [7] observed that in a solitary breaking wave, a downburst of turbulence descends and diverges at the bed creating two counter-rotating vortices. More recently, Lubin et al. [24] numerically simulated plunging breaking waves and their results confirmed what shown in a rare documentary footage where breaking waves were recorded from underwater. In fact, they computed 3D vortical tubes, like vortex filaments elongated in the main flow direction, occurring under the plunging breaker, connecting the splash-up and the main tube of air. Lubin et al. [25] recently observed them also experimentally. Furthermore, Mukaro [26] observed that instantaneous vorticity tended to organize into thin filaments of counter-rotating pairs.

Therefore, it is evident that further experimental investigation on coherent events is still needed, in the attempt to better clarify these mechanisms of turbulence spreading due to wave breaking. This is the motivation of the present study, which investigates the surf zone of two laboratory regular waves, a plunging one and a spilling one, propagating on a fixed and impermeable slope in a 2D wave flume. The measurements were carried out by means of a Laser Doppler Anemometer (LDA) in some selected channel sections, located in the outer and inner surf zone. At the same time and locations, the elevation data were also acquired using a resistive probe. It is worth noting that, compared with previous research described above, the present work differs in particular for the measurement instrumentation adopted and the analyzed target region. Moreover, here the principal characteristics are discussed in terms of turbulent kinetic energy and turbulent intensities, length scales and coherent motions, for both spilling and plunging breaking, with the aim of contributing to a better understanding of turbulence dispersion. In this way, the conceptual models that describe typical engineering applications in coastal areas could benefit from this research.

2. Materials and Methods

2.1. Experimental Set Up

The present experiment was carried out in the wave flume of the Department of Civil, Environmental, Land, Building Engineering and Chemistry (DICATECh) of the Polytechnic University of Bari (Italy). The flume was 45 m long, 1 m wide and 1.20 m deep, provided with glass sidewalls and bottom (Figure 1). A fixed and uniform slope 1:20 was created in the channel, starting 12 m from the paddles. The slope was 33 m long. The still water level in the channel was $h_0 = 0.7$ m above the horizontal bed. The examined regular waves had heights H at the paddle respectively equal to 10 cm and 7 cm. Breaking occurred at a depth of about 11 cm for both tests. The plunging wave case, named

Test_P, is characterized by a Irribarren number ξ_0 equal to 0.6, while the spilling wave case, named Test_S, by $\xi_0 = 0.2$ (see [2] for details).

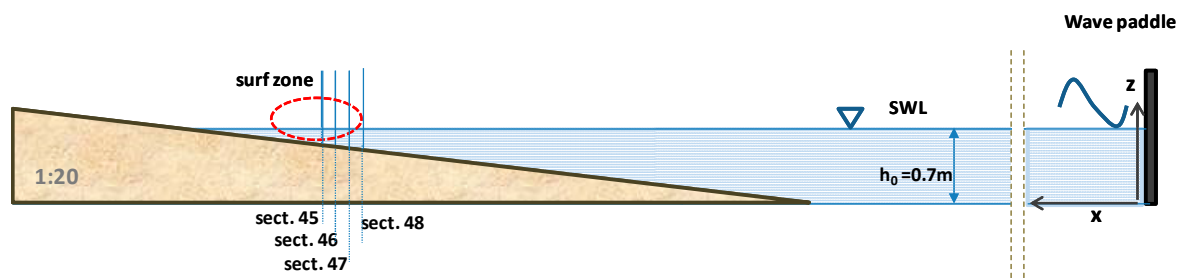


Figure 1. Sketch of the wave flume, with the location of the examined vertical sections.

The measurements were carried out in some selected channel sections in the shoaling and in the breaking zone, for both tests. In the present study, four vertical sections close to the breaking region (identified as section 48, section 47, section 46 and section 45, in Figure 1) are examined. Specifically, section 48 was in the prebreaking region, section 47 was where the incipient breaking occurred, while in sections 46 and 45, the wave re-arranged into a bore. The horizontal reference system x has origin at the wave paddle and is positive towards the shore, while the vertical axis z has origin on the bottom and is positive upwards. The locations and local depths h for sections 48, 47, 46 and 45 are displayed in Table 1. In the same table, the wave height H , the wave period T , the length computed according to Airy theory L_A , and the Ursell parameter, an indicator of the wave non-linear behavior, are also shown.

Table 1. Main characteristics of the two tested regular wave trains.

TEST	Sect.	x [m]	h [cm]	H [cm]	T [s]	L_A [m]	Ur	Measurements Range [cm]
Test_P plunging	48	22.9	14	12.64	4	4.66	1000	$z = 1-11$
	47	23.3	11.3	9.67	4	4.19	1177	$z = 1.3-8.3$
	46	23.7	10	7.02	4	3.72	970	$z = 2-8$
	45	24.1	8.5	5.98	4	3.17	976	$z = 1.5-7$
Test_S spilling	48	22.9	14	6.78	1	1.06	27.88	$z = 1-12$
	47	23.3	11.3	6.62	1	0.97	43.58	$z = 3.3-9.3$
	46	23.7	10	5.52	1	0.89	43.74	$z = 1-8$
	45	24.1	8.5	4.21	1	0.78	41.94	$z = 1-7.5$

The instantaneous horizontal u and vertical w velocities, respectively measured along the longitudinal x and the vertical z axis, were assessed by means of a 2D back-scatter, four-beam LDA along the water column. These velocities are conventionally established positive if respectively directed onshore and upwards. The acquisition frequency of the LDA was mainly approximately 100 Hz and the duration of each measurement was at least 200 s, thus permitting sufficient wave cycles (on average 50) to use in the subsequent phase-averaging procedure. At the same time, a resistive wave gauge aligned with the LDA volume of measurement was used to measure the surface elevation. In each section, the velocities were assessed vertically in points spaced 0.5 cm or 1 cm, depending on local conditions (Table 1).

The used LDA instrumentation could provide a single point measurement, differently from the more sophisticated instrumentation, i.e., PIV [1,17] and Volumetric 3V [20,22], which instead provided measurements respectively in 2D slices and 3D volumes, thus allowing a direct description of a large portion of the flow field. In any case, the data processing allowed the indirect detection of the main turbulent structures, as observed in previous studies. Moreover, it is worth noting that the sampling

frequency of the adopted LDA system is much greater than that of the PIV and V3V systems utilized in previous research (ranging from 7.5 Hz to 15 Hz). This aspect is fundamental because it guarantees to better capture the turbulent behavior of the phenomenon at higher frequencies.

2.2. Operational Procedure

Several techniques can be used to extract eddies in a flow field [7,27], including: direct analysis of the vorticity field as computed from velocity map; analysis of the velocity gradient tensor which has one imaginary eigenvalue whose distribution is associated with regions of local swirling motion; LES filtering, based on low pass filtering of velocity data to remove small scale contributions; wavelet transform algorithms of the velocity vector field; quadrant analysis.

The present study first used the phase-averaging procedure (i.e., the most common notation for periodic signal processing) to extract the turbulent velocity components from the instantaneous velocity time series [3,28]. As well known, the instantaneous signal can be regarded as the sum of a time-averaged part (addressed with the capital letter), a phase-averaged or orbital part (addressed with the subscript *ph*) and a turbulent fluctuation (addressed with the prime sign). As an example, for the horizontal velocity, being *t* the variable time, it can be written as:

$$u(t) = U + u_{ph}(t/T) + u'(t) \quad (1)$$

After this, the focus is on the quadrant analysis to identify the coherent motions and quantify the bursting processes in the instantaneous turbulent velocity time series, based on [29]. The decomposition of the turbulent Reynolds shear stress $u'w'$ (apart from $-\rho$, water density) is considered into four quadrants defined by the Cartesian axes of the scatter plot $w' = f(u')$. The quadrants identify four types of events: (Q1) outward interactions, $u' > 0$ and $w' > 0$; (Q2) ejections, $u' < 0$ and $w' > 0$; (Q3) inward interactions, $u' < 0$ and $w' < 0$; (Q4) sweeps, with $u' > 0$ and $w' < 0$. Associated with the bursting process are ejections, where low-speed fluid penetrates the high flow region, and sweeps, where the high-speed fluid penetrates the low flow region [30]. Both ejections and sweeps contribute positively to the Reynolds stress. An event is included in the consideration if the product $u'w'$ is larger than a critical threshold, otherwise it is discarded as noise. Setting this threshold is somewhat arbitrary.

Therefore, based on previous research [29], the coherent event has been defined as the one responding to the following condition: $|u'w'| \geq (\mu + \sigma)$, where μ is the mean and σ the standard deviation of the $u'w'$ time series measured in the investigated point. Analogously, an intense coherent event is detected when $|u'w'| \geq (\mu + 3\sigma)$.

3. Results and Discussion

3.1. Phase-Averaged Distributions

To provide an insight in the flow field, Figure 2 sketches the phase-averaged velocities (u_{ph} , w_{ph}) in a wave cycle, at the depths examined in Test_P (Figure 2a) and Test_S (Figure 2b) in section 47, i.e., where the breaking is incipient. The scale of the velocities is the same in both Figure 2a,b. Since no noticeable deformation of the wave shape is observed through propagation over a distance of one wavelength, at least offshore the measuring section, the horizontal axis in Figure 2 (showing the instant time in the period) may be regarded approximately as the horizontal spatial coordinate in the wavelength [7,15].

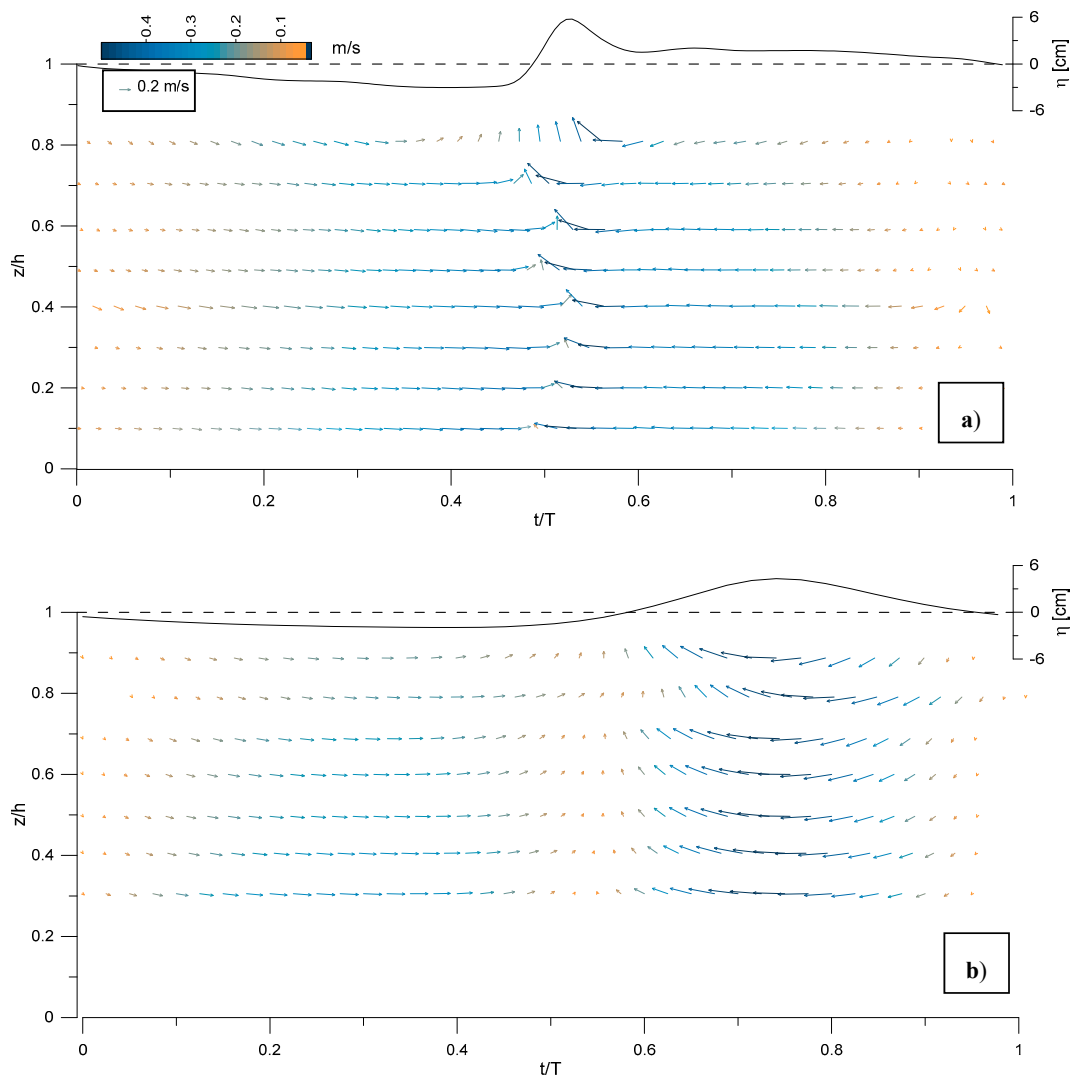


Figure 2. Section 47: phase-averaged velocities (u_{ph} , w_{ph}) in the wave cycle at all investigated depths for (a) Test_P and (b) Test_S.

In the upper part of each plot is also added the phase-averaged elevation η . A difference is immediately noticed in the vertical asymmetry of the incipient breaking wave between the two tests. As expected, in Test_P the wave crest is higher while the wave trough is lower than in Test_S. Moreover, the horizontal asymmetry highlights that in Test_P, the steep plunging breaker occupies a much more limited portion of the wavelength, compared to the case of the spilling breaker. Nevertheless, the distribution along the wave cycle of the phase-averaged velocities, plotted in Figure 2 as vectors with components (u_{ph} , w_{ph}), is quite similar for Test_P and Test_S. Indeed, it resembles the wave elevation trend in both tests, with increasing velocities in the transition trough-crest (ascending phase) and decreasing velocities in the transition crest-trough (descending phase), at all depths. As well, a rotation of the velocity vectors is observed in the wave cycle at all depths, for both tests, coherently with the curvature of the surface, as already noted in previous experiments [7,31]. Consequently, during the first descending phase, the velocities are fairly uniformly oriented downwards and offshore, while in the accelerating phase, they rotate upward and onshore. In the plunging wave (Figure 2a) below the wave crest, the maximum velocity value is noted, which is quite vertical in the most superficial layer. In the spilling case (Figure 2b), below the crest, onshore horizontal velocity is observed at all depths. The reduction in the velocity values (absolute values) from the surface to the bottom is more marked in Test_P (Figure 2a) than in Test_S (Figure 2b).

Referring to the same section 47, it is worth depicting the distribution in the wave cycle of the turbulence intensities u'_{ph} and w'_{ph} , computed by definition as the square root of $(u'^2)_{ph}$ and $(w'^2)_{ph}$. Figure 3a provides the turbulence intensities for Test_P, showing that the horizontal ones are higher than the vertical ones, as well as their decrease from surface to bottom, consistently with the incipient breaking. They both have their peak at the lower edge of the eddy region, also in accordance with Nadaoka et al. [15]. Moreover, the tail of the contour lines is slightly oriented downwards and offshore, thus endorsing the possible presence of obliquely descending eddies (ODEs) numerically and experimentally proved by Lubin [10,24].

Figure 3b displays u'_{ph} and w'_{ph} values for Test_S, highlighting that in the spilling case they are approximately one third of those measured in Test_P. Furthermore, in this case, the u'_{ph} values are greater than the w'_{ph} values and they both reduce towards the bottom. The highest values for u'_{ph} are localized under the ascending and descending phases of the wave, while the highest values for w'_{ph} are localized under the crest. These patterns seem consistent with the propagating spilling bore. It is worth noting the recursive occurrence for both the tests of the turbulence intensities along the wave phases, thus stating an organized turbulent structure, which is quite typical for plunging and spilling waves.

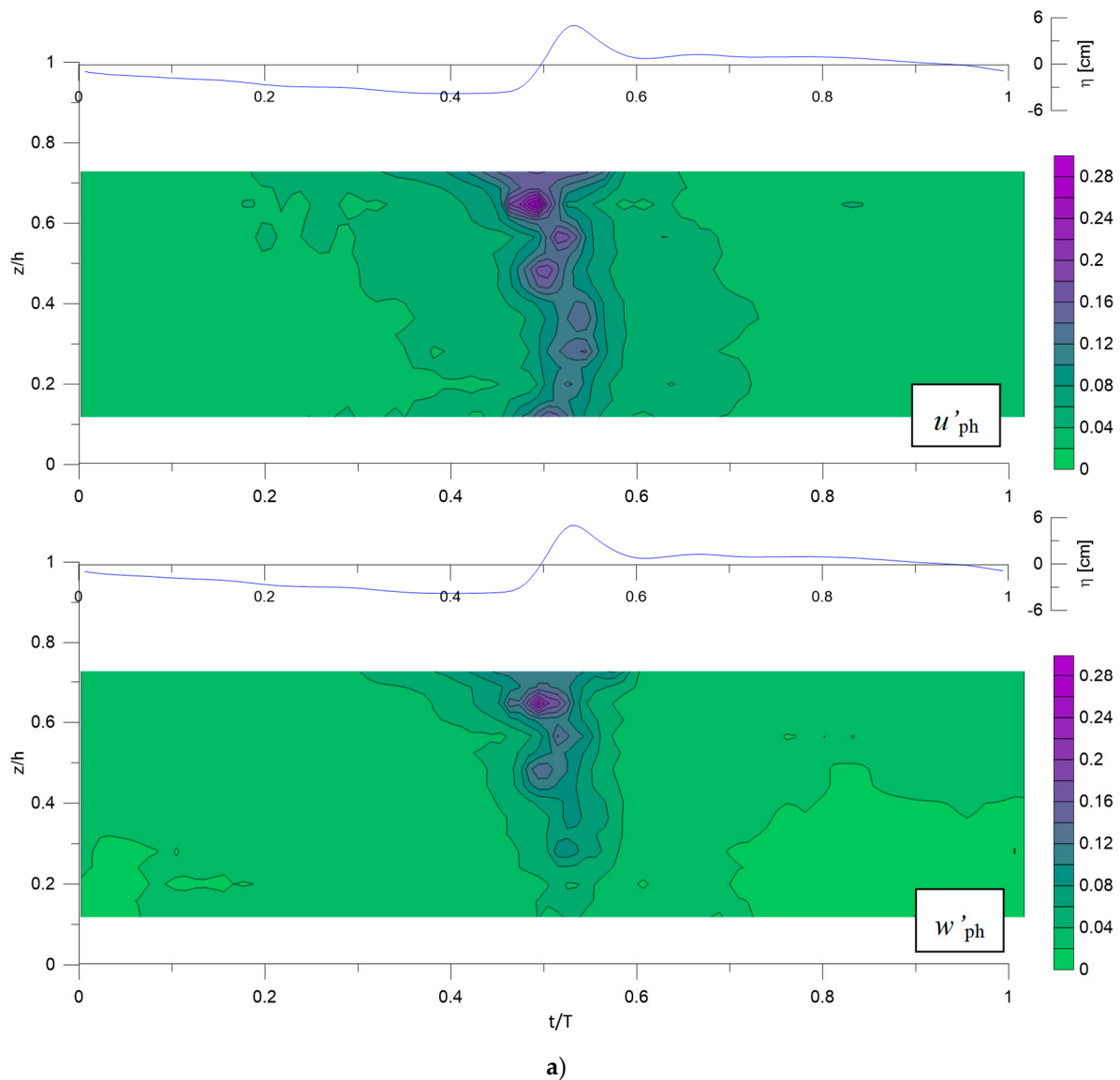


Figure 3. Cont.

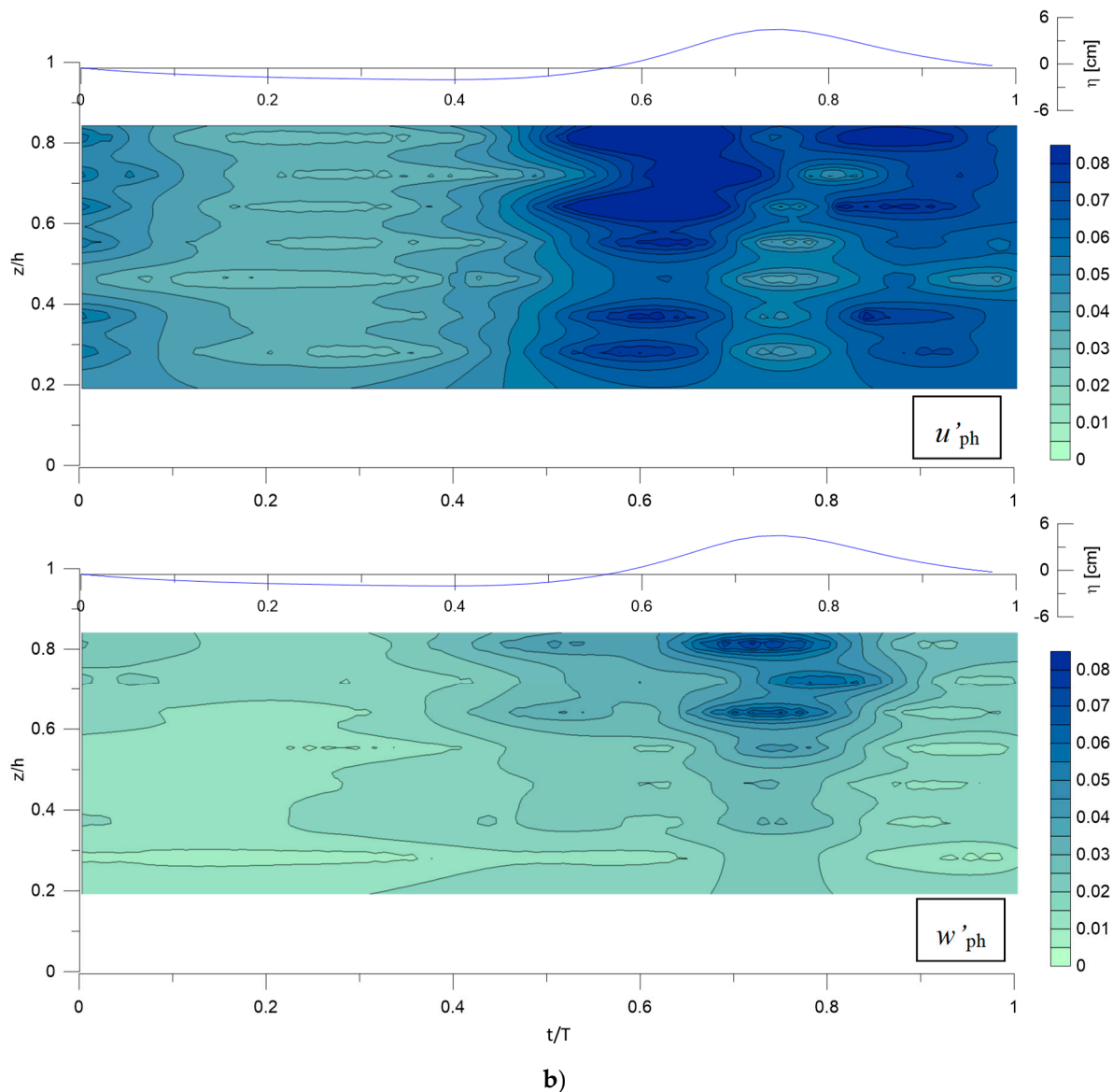


Figure 3. Section 47: phase-averaged turbulent intensities in the wave cycle at all the investigated depths: (a) u'_{ph} and w'_{ph} for Test_P; (b) u'_{ph} and w'_{ph} for Test_S. Units are in m/s.

3.2. Time-Averaged Profiles

The vertical profiles of the time-averaged turbulent Reynolds shear stresses $U'W'$ and of the turbulent kinetic energy K are examined in sections 48, 47, 46 and 45. For Test_P, they are respectively shown in Figure 4a,b, where the plotted points refer to the locations below the still water level.

The turbulent Reynolds stresses $U'W'$ in Figure 4a are quite negligible for sections 48 and 47, excepting the lowest point of section 48, in the boundary layer streaming, where the $U'W'$ value is positive, coherently with the effect of the bottom boundary layer. Referring in particular to section 47, the small order of magnitude of the $U'W'$ stresses (Figure 4a) can be compared with the higher one of the u'_{ph} and w'_{ph} shown in Figure 3a. It can be deduced that the major contribution to the total turbulent Reynolds stress in the incipient breaking (section 47) is essentially due to the phase-averaged turbulent velocities.

In section 46, immediately after the breaking, the $U'W'$ stresses are negative near the surface, and almost zero in the underlying region. In section 45 where the wave is reforming, they assume negative values near the surface and the highest positive values in the intermediate and lower part. This vertical gradient of $U'W'$ suggests a downward transport of turbulence from the surface, due to

the occurred plunger [3,28], which is more evident in the upper region, for $z/h > 0.4$ in both sections 46 and 45. The largest positive $U'W'$ stresses are present in section 45, when the wave has formed again, near the bottom, proving that the effects of the bottom boundary layer are again felt [3,28,31].

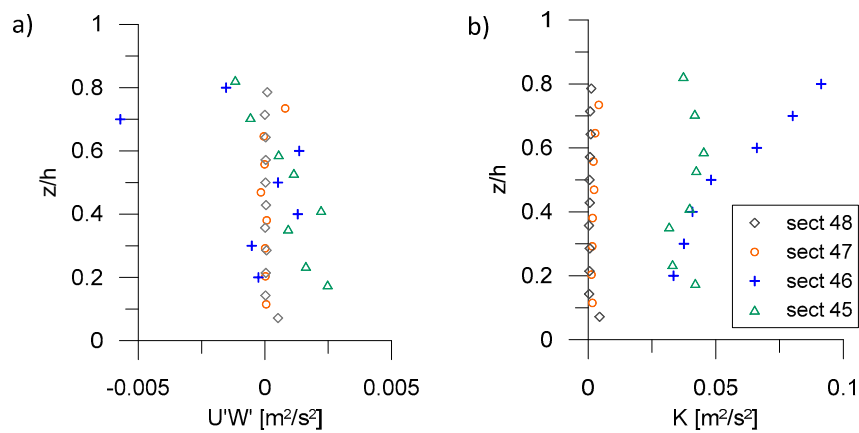


Figure 4. Test_P: vertical profiles of the time-averaged turbulent Reynolds stresses (a) and turbulent kinetic energy (b).

The different behavior between the prebreaking/incipient breaking sections (sections 48 and 47) and the sections shoreward the breaking (sections 46 and 45) is also evident in the vertical trends of the time-averaged turbulent kinetic energy K , here computed following Svendsen [32]. In fact, it tends to zero in sections 48 and 47 (Figure 4b), while its highest values are assessed in section 46, especially for $z/h > 0.5$ due to the reversed plunger, where a decreasing trend towards the bottom is noted, meaning a spreading downward as in [1]. Analogously, also in section 45, the K profile has a similar shape, but the surface values are lower than in section 46, considering that the turbulence is decreasing with the increasing distance from the plunging breaker, meaning spreading downstream, in accordance with [1].

These observations are consistent for Test_P with the vertical distributions of the time-averaged integral length scales, L_x and L_z , associated with the turbulent large eddies (Figure 5a,b) respectively in x and z directions. The integral and turbulent length scales have been computed by multiplying the local time-averaged velocity respectively for the turbulent time scale and the integral time scale. In turn, both turbulent and the integral time scales have been estimated based on the temporal autocorrelation function of the turbulent velocity fluctuations (for the detailed formulation, please refer to [33]). It is noteworthy that the integral length scales L_x , while having order $O(0.1 h)$ in both sections 48 and 47 and 46, tend to be of order $O(0.2 \div 0.3 h)$ in section. 45, thus proving that large eddies are stretched in the x direction, as a consequence of the breaking.

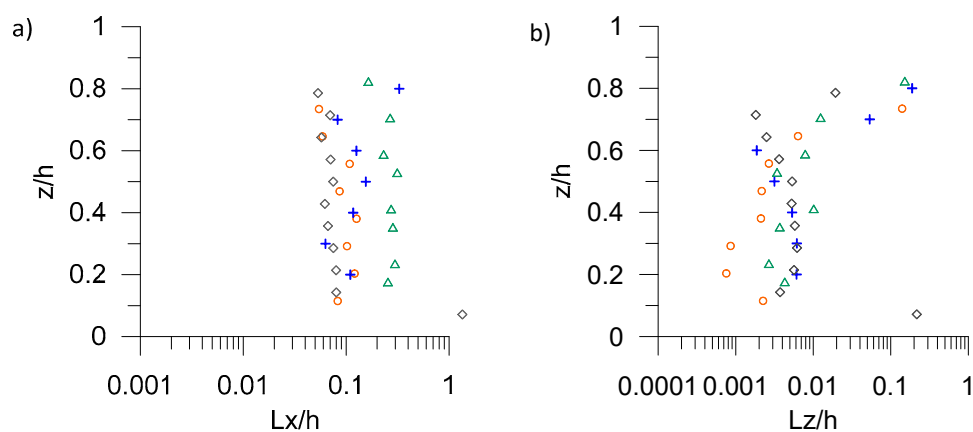


Figure 5. Cont.

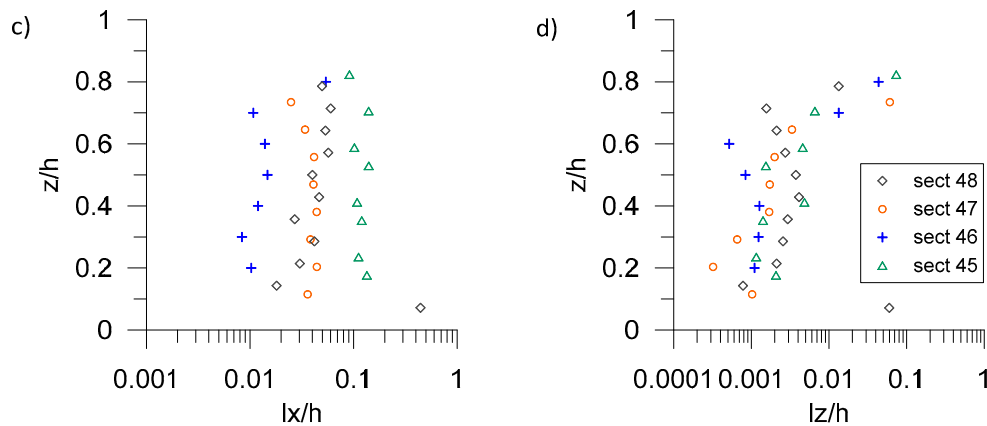


Figure 5. Test P: time-averaged horizontal (a) and vertical (b) integral length scales; time-averaged horizontal (c) and vertical (d) turbulent length scales.

Moreover, by comparing Figure 5a,c, it can be deduced that in sect. 46, immediately after the breaking, the l_x scales are one order lower than the L_x scales. The same is also noted referring to the vertical L_z and l_z scales (Figure 5b,d), thus confirming the transfer of the energy contained at large scales to small scales, where it is turned into heat by viscosity [7]. Moreover, for $z/h > 0.6$ both L_z and l_z scales show increasing values as they approach the surface, with order ranging from $O(0.01 h)$ up to $O(0.1 h)$, consistently with the formation of the overturning plunging jet.

The same analysis of the time-averaged quantities has been performed also for Test_S. Analogously to Test_P, the $U'W'$ stresses are quite negligible in sections 48 and 47 (Figure 6a). In section 46, when the spilling wave has just broken, there is a uniform positive trend along the z -axis. Onshore, in section 45, the $U'W'$ profile shows the same bi-triangular shape already noted in Test_P (Figure 4a), although in this case, lower positive values are displayed near the bottom and higher negative values for $z/h > 0.3$.

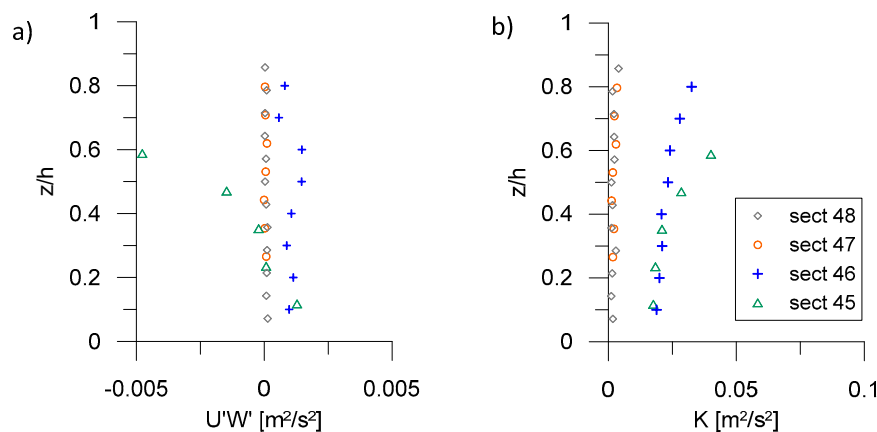


Figure 6. Test_S: vertical profiles of the time-averaged turbulent Reynolds stresses (a) and turbulent kinetic energy (b).

Furthermore, the distribution of K (Figure 6b) shows vertical trends already observed in Test_P, with decreasing values from the surface towards the bed in both sections 46 and 45. Nevertheless, in Test_S, the values of K are halved with respect to Test_P. Moreover, the higher values of K are observed in section 45, based on the presence of the bore after spilling, rather than in section 46. Comparing Figure 6a,b with Figure 4a,b, it can be assumed that with the bore propagating onshore, the spilling breaker continues to feed turbulence in the surface region, unlike the plunging wave, which produces higher turbulence but is located in a more compact area, where the breaking occurs. Moreover, the turbulent kinetic energy is less intense in the spilling case than in the plunging case.

Referring to the time-averaged integral length scales L_x and L_z (Figure 7a,b), for each section there is a difference of approximately two orders of magnitude between them, proving the presence of eddies much more elongated in the horizontal direction than in the vertical direction. This horizontal stretching is thus greater for this spilling case than for the plunging one. Referring to the turbulent length scales l_x and l_z for Test_S, although they are lower than the corresponding integral ones, l_x has a comparable order of magnitude with L_x and the same thing happens when comparing l_z and L_z . Consequently, their graphs are not shown for brevity, being of little significance especially in the semi-logarithmic version. In any case, it is worth noting that despite eddies could not be observed directly, as for example in [1,17,20,22] based on PIV or V3V acquisitions, the distributions of these length scales permitted the indirect deduction of the presence of eddies in the target domain.

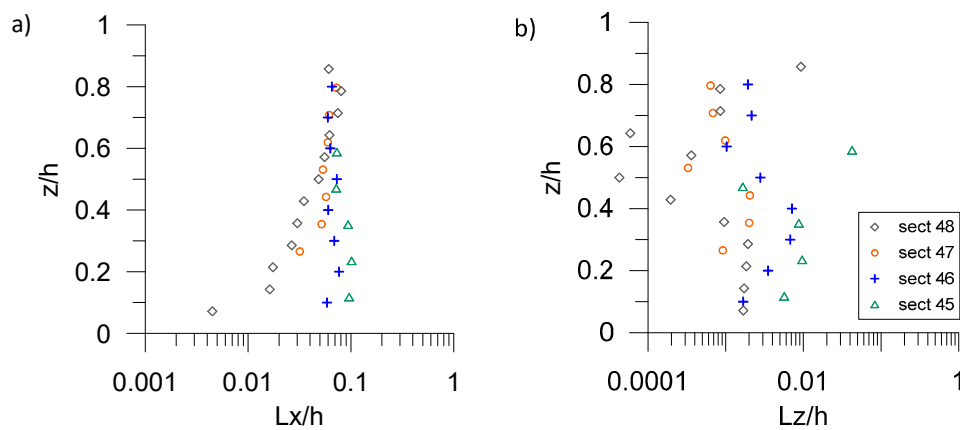


Figure 7. Test_S: time-averaged horizontal (a) and vertical (b) integral length scales.

3.3. Quadrant Analysis

The results of the quadrant analysis are here described only referring to section 47, for the sake of brevity, for both Test_P (Figure 8) and Test_S (Figure 9). Figures 8 and 9 display the quadrant plots of the instantaneous turbulent velocities (u' , w') at five different phase intervals. The phases for which the data are plotted are written for each plot and have been selected based on meaningful parts along the wave cycle. Namely, for Test_P (Figure 8): $0 < t/T < 0.4$ descending phase; $0.4 < t/T < 0.6$ descending phase up to wave trough; $0.6 < t/T < 0.65$ ascending phase up to wave crest; $0.65 < t/T < 0.75$ steep descending phase; $0.75 < t/T < 1$ flat descending phase. Analogously, for Test_S (Figure 9): $0 < t/T < 0.2$ descending phase; $0.2 < t/T < 0.4$ flat descending up to wave trough; $0.4 < t/T < 0.6$ gradual ascending phase; $0.6 < t/T < 0.8$ ascending phase up to wave crest; $0.8 < t/T < 1$ descending wave back. The phase-averaged wave elevation is also inserted in both figures to facilitate the identification of the abovementioned phase intervals. Further, the results in the top row refer to a near surface point, while those in the bottom row to a near bottom point. The scaling for the axes is the same for an easier comparison, except the interval 0.6–0.75 in Test_P (Figure 8) due to high turbulent velocities.

The top row of Figure 8 shows that in section 47 for the point at $z/h = 0.7$, the turbulent horizontal fluctuations u' are the largest during the ascending phase $0.6 < t/T < 0.65$ (confirming [29]) and under the wave crest $t/T = 0.65$. On the contrary, they are minimal in the descending phase ($0.65 < t/T < 0.75$), where the turbulent vertical fluctuations w' prevail and are the largest. In the remaining wave cycle, i.e., for $0 < t/T < 0.6$ and $0.75 < t/T < 1$, the plots tend to assume a quite circular shape, meaning that the ($u'w'$) points are fairly evenly distributed in all the quadrants Q1 ÷ Q4. For $0.4 < t/T < 0.6$, the cloud of points is slightly elongated along the horizontal axis, thus the u' components prevail. For $0.75 < t/T < 1$ the cloud of points is slightly aligned along Q2 and Q4 quadrants, proving the presence of ejections and sweep after the wave crest passage.

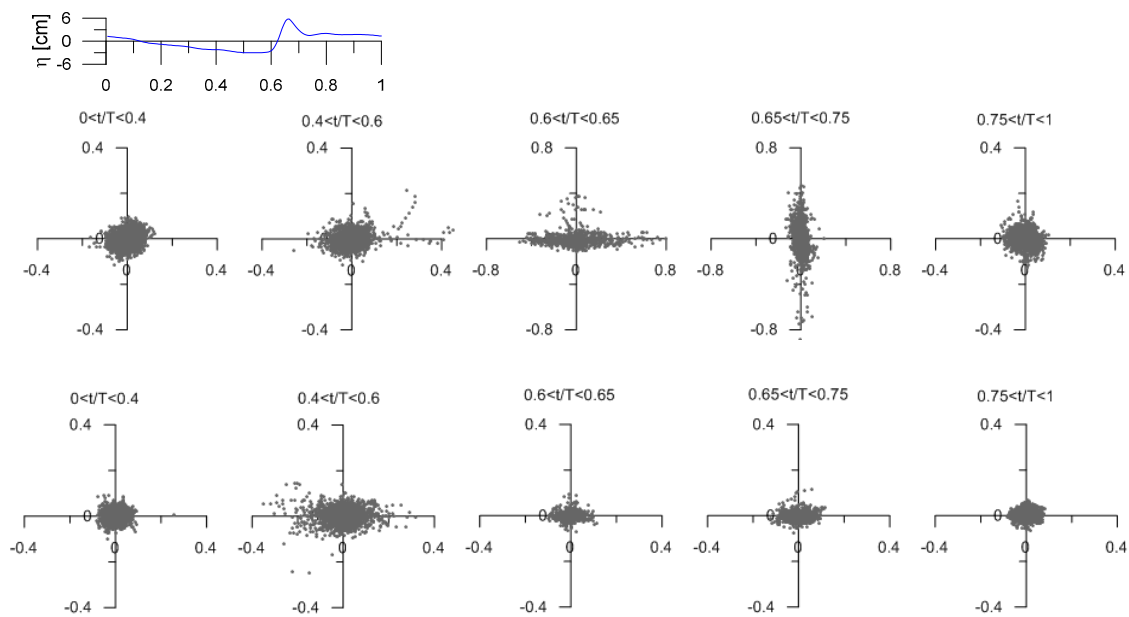


Figure 8. Test_P, sect. 47: quadrant plots in five phase intervals, at $z/h = 0.7$ (top row) and $z/h = 0.2$ (bottom row).

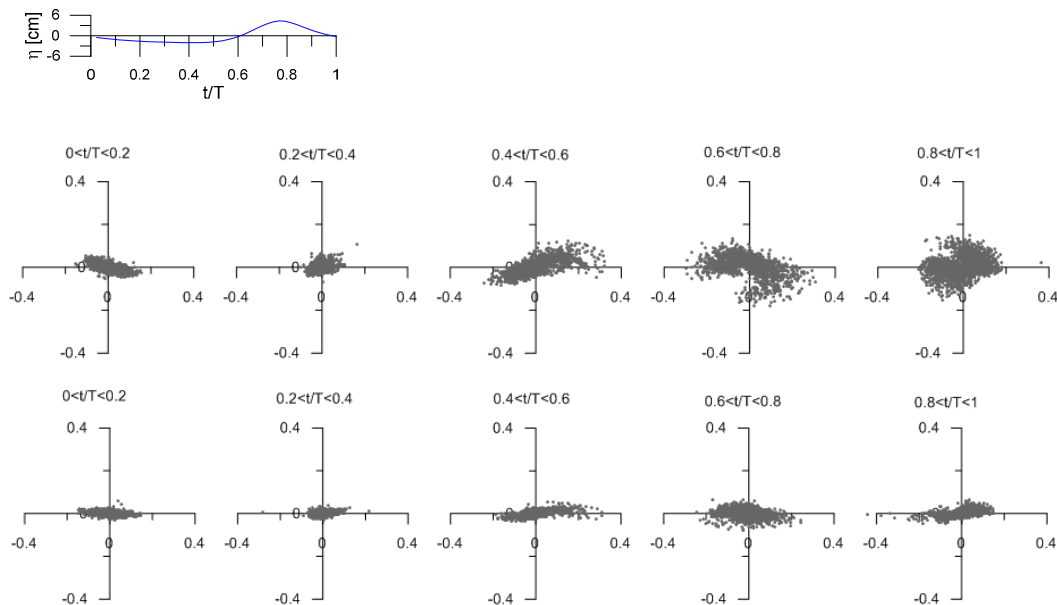


Figure 9. Test_S, section 47: quadrant plots in five phase intervals, at $z/h = 0.7$ (top row) and $z/h = 0.3$ (bottom row).

The bottom row of Figure 8, referring to the point at $z/h = 0.2$ in section 47, depicts generally flattened plots. This is consistent with the presence of the bottom, reducing w' even if a large eddy due to wave breaking reaches the bottom boundary, as also noted in [29]. The u' in $0.6 < t/T < 0.75$ are much smaller than the corresponding ones near the surface, meaning that the passage of the wave crest has a negligible effect near the bottom. On the contrary, increasing values of u' near the bottom are noted rather than near the surface, during the descending phase and below the wave trough ($0.4 < t/T < 0.6$). From this analysis, a recursive tendency of the bursts in the wave cycle is evident, especially in the superficial layer, referring to the trough-crest transition and to the descending phase, under the back face of the wave.

The top row of Figure 9 displays the quadrant analysis assessed for the spilling case (Test_S) in section 47, referring to the point at $z/h = 0.7$. In the descending phase $0 < t/T < 0.2$, the plot is sloped

along Q2–Q4 quadrant, proving the presence of both ejections and sweeps. In the region approaching the trough ($0.2 < t/T < 0.4$), turbulent intensities reduce strongly, while they increase again during the ascending phase ($0.4 < t/T < 0.6$) where both outward and inward motions are noted (cloud deployed along Q1–Q3 quadrant). During the ascending phase up to the wave crest ($0.6 < t/T < 0.8$), the plot is directed along Q2–Q4, with the presence of ejections and sweeps, already noted in Figure 3b. In the back face of the wave ($0.8 < t/T < 1$), again both the inward and outward motions are relevant (Q1–Q3).

Similar to the bottom row of Figure 8, also in the bottom row of Figure 9, referring to the point at $z/h = 0.3$, there are flattened clouds, which indicate the effect played by the bottom on the w' velocities. Furthermore, the largest w' values during the interval $0.6 < t/T < 0.8$ are noted, when the crest is approaching. The largest u' values are observed in the transition trough-crest-trough ($0.4 < t/T < 1$). In the case of the spilling wave, the quadrant analysis highlights a dependence of the bursts on the wave phases even more marked with respect to the plunging case. Although different from the plunging case, in the spilling case, this effect is strongly noted close to the surface as well as close to the bottom.

Finally, the authors detected the coherent events, according to the method described in Section 3.2. For both Test_P and Test_S, in each examined section, for three points (near surface, intermediate, near bottom), the assessed time series of $u'w'$ have been analyzed. The mean and the standard deviation were computed for each considered $u'w'$ signal and then the number of cases for which $|u'w'| \geq (\mu + \sigma)$ were detected, thus identifying the coherent events in the series. The same has been made for detecting the most intense coherent events, for the condition $|u'w'| \geq (\mu + 3\sigma)$ [24].

Table 2 summarizes the results for the most significant sections, i.e., sections 47, 46 and 45. In the last two columns, the authors indicate: the percentage of coherent events %CE i.e., the number of data for which $|u'w'| \geq (\mu + \sigma)$, rated by the total number of the acquired data, as well, the percentage of intense coherent events %IE, i.e., the number of data for which $|u'w'| \geq (\mu + 3\sigma)$, rated by the total number of the acquired data.

Table 2. Coherent and intense coherent events detected for TEST_P and TEST_S by means of the threshold values for the signal $u'w'$.

TEST_P				TEST_S			
Sect.	z/h	%CE	%IE	Sect.	z/h	%CE	%IE
47	0.7	3.2	1.1	47	0.8	13.6	2.6
47	0.5	2.9	1.1	47	0.4	13.3	2.2
47	0.2	7.4	1.9	47	0.3	12.5	2.2
46	0.7	10.5	1.6	46	0.7	22.5	1.4
46	0.5	7.5	1.2	46	0.5	24.7	1.6
46	0.2	5.5	1.1	46	0.3	21.8	1.6
45	0.7	12.3	1.8	45	0.5	18.6	2.3
45	0.5	13.7	1.7	45	0.2	20.0	1.6
45	0.2	11.9	1.7	-	-	-	-

For Test_P, the following can be noted. In section 47, the percentage of both coherent and intense coherent events increases from the surface towards the bottom. On the contrary, immediately after breaking in section 46, both percentages of coherent and intense coherent events, decrease with depth.

In section 45, the %CE percentage is the highest at the intermediate depth, while the %IE percentage remains quite unchanged at all depths. The comparison between sections 46 and 45 leads to thoughts of a spreading of the coherent events towards the bottom, while the intense ones are more localized in the upper layer, which is consistent with the splashed jet.

For Test_S, in section 47 the percentage of both coherent and intense coherent events decreased from the surface towards the bottom, being opposite to what was observed in Test_P in the same section, and presumably due to the formation of the roller. In section 46, the maximum %CE percentage is at

mid-depth, while the %IE percentage tends to increase with depth. In section 45, the %CE percentage increases towards the bottom, while the %IE percentage decreases towards the bottom. It could be argued from the comparison of percentages in section 47 and 46 that in this case, the coherent and intense coherent events, initially more localized around the spiller, are spread downwards and onshore, thus affecting also section 45. The percentages computed are comparable with previous results [23,30].

Finally, it is observed that in Test_P, coherent and intense coherent events are more infrequent, especially referring to sections 46 and 45, where the percentages for Test_S are 2–3 times higher than in Test_P. This could be explained by the different breaking mechanism and the different nature of generated turbulence that characterize the two waves, especially considering the non-deterministic nature of a splashing jet.

4. Conclusions

Two regular breaking waves, a spiller and a plunger, reproduced in a laboratory wave flume have been examined. Specifically, this study focused on the turbulent structure induced by their breaking in the surf zone. By separating time-averaged velocities, phase-averaged velocities and turbulent velocities, as well as by adopting the quadrant analysis, turbulent eddies and coherent bursts were detected. The principal results of the study are summarized below.

The distribution along the wave cycle of the phase-averaged velocities at breaking is similar for both plunging and spilling cases, considering that their trends resemble the wave elevation, despite the nonlinear behavior in the surf zone, with increasing velocities in the transition trough-crest and decreasing velocities in the transition crest-trough at all depths. The rotation of the velocity vectors in the wave cycle at all depths is also noted coherently with the curvature of the surface and in agreement with previous experiments [7,31]. The pattern of the phase-averaged turbulence intensities at the incipient breaking highlights for both plunging and spilling cases that the horizontal ones are greater with respect to the vertical ones, as well as their decrease from surface to bottom, as expected. Rather, for the plunging case, these turbulence intensities spread downwards and offshore, thus endorsing the possible presence of obliquely descending eddies proved in previous studies [10,15,24].

For both plunging and spilling waves, the vertical profiles of the time-averaged turbulent Reynolds shear stresses show that they are fairly negligible in the prebreaking and incipient breaking region, while they assume relevance in sections immediately after breaking, showing a vertical gradient that suggests a downward transport of turbulence from the surface. The vertical trends of the time-averaged K display that turbulence is higher in the plunger than in the spiller, but it decreases with increasing depth as well as with increasing distance from the breaking section. Differently, the bore propagating onshore the spilling breaker seems to feed turbulence in the surface region also onshore on the breaking section. The different order of magnitudes of the time-averaged integral and turbulent length scales onshore breaking confirms that the energy contained at large scales is transferred to small scales. Furthermore, these values (breaking onshore) prove the presence of eddies much more elongated in the horizontal direction than in the vertical one. This horizontal stretching is greater for the spilling case than for the plunging case.

Finally, the quadrant analysis has been executed to detect coherent events, recurring in the wave cycle. For both the plunging and the spilling test, a reduction of the intensities of the bursts is evident from the surface towards the bottom. In the plunging wave, maxima horizontal u' values are noted in the ascending phase of the wave, and maxima vertical w' values in the descending phase, when the breaking is incipient. In the spilling case, there are greater turbulent bursts corresponding to ejections and sweeps mainly during the ascending phase and below the crest of the wave. Different from the plunging case, in the spilling the dependence of the bursts on the wave phases is strongly noted close to the surface as well as close to the bottom. By examining the number of coherent and intense coherent events based on a previous study [29], it can be argued that, due to the different breaking mechanism, the spilling case is dominated by coherent events while in the plunging case, the splashing jet has a much more non-deterministic nature, thus inducing less frequent coherent events.

Author Contributions: Conceptualization and methodology F.D.S. and M.M.; data analysis and writing, F.D.S.; review and editing, F.D.S. and M.M.

Funding: This research received no external funding.

Acknowledgments: The technical staff of the laboratory at DICATECh is gratefully acknowledged.

Conflicts of Interest: The authors declare no conflicts of interest.

References

1. Kimmoun, O.; Branger, H. A particle images velocimetry investigation on laboratory surf-zone breaking waves over a sloping beach. *J. Fluid Mech.* **2007**, *588*, 353–397. [[CrossRef](#)]
2. De Serio, F.; Mossa, M. Experimental study on the hydrodynamics of regular breaking waves. *Coast. Eng.* **2006**, *53*, 99–113. [[CrossRef](#)]
3. De Serio, F.; Mossa, M. A laboratory study of irregular shoaling waves. *Exp. Fluids* **2013**, *54*, 1536. [[CrossRef](#)]
4. De Padova, D.; Brocchini, M.; Buriani, F.; Corvaro, S.; De Serio, F.; Mossa, M.; Sibilla, S. Experimental and Numerical Investigation of Pre-Breaking and Breaking Vorticity within a Plunging Breaker. *Water* **2018**, *10*, 387. [[CrossRef](#)]
5. Van der Zanden, J.; van der A, D.A.; Cáceres, I.; Hurther, D.; McLelland, S.J.; Ribberink, J.S.; O'Donoghue, T. Near-Bed Turbulent Kinetic Energy Budget Under a Large-Scale Plunging Breaking Wave Over a Fixed Bar. *J. Geophys. Res. Oceans* **2018**, *123*, 1429–1456. [[CrossRef](#)]
6. Van der A, D.A.; van der Zanden, J.; O'Donoghue, T.; Hurther, D.; Cáceres, I.; McLelland, S.J.; Ribberink, J.S. Large-scale laboratory study of breaking wave hydrodynamics over a fixed bar. *J. Geophys. Res. Oceans* **2017**, *122*, 3287–3310. [[CrossRef](#)]
7. Ting, F.C.K. Large-scale turbulence under a solitary wave: Part 2. Forms and evolution of coherent structures. *Coast. Eng.* **2008**, *55*, 522–5368. [[CrossRef](#)]
8. Zhou, Z.; Sangermano, J.; Hsu, T.J.; Ting, F.C.K. A numerical investigation of wave-breaking-induced turbulent coherent structure under a solitary wave. *J. Geophys. Res. Oceans* **2014**, *119*, 6952–6973. [[CrossRef](#)]
9. Farahani, R.J.; Dalrymple, R.A. Three-dimensional reversed horseshoe vortex structures under broken solitary waves. *Coast. Eng.* **2014**, *91*, 261–279. [[CrossRef](#)]
10. Lubin, P.; Glockner, S. Numerical simulations of three-dimensional plunging breaking waves: Generation and evolution of aerated vortex filaments. *J. Fluid Mech.* **2015**, *767*, 364–393. [[CrossRef](#)]
11. Longo, S. Vorticity and intermittency within the pre-breaking region of spilling breakers. *Coast. Eng.* **2009**, *56*, 285–296. [[CrossRef](#)]
12. Huang, Z.C.; Hwung, H.H.; Chang, K.A. Wavelet-based vortical structure detection and length scale estimate for laboratory spilling waves. *Coast. Eng.* **2010**, *57*, 795–811. [[CrossRef](#)]
13. Lim, H.J.; Chang, K.A.; Huang, Z.C.; Na, B. Experimental study on plunging breaking waves in deep water. *J. Geophys. Res. Oceans* **2015**, *120*, 2007–2049. [[CrossRef](#)]
14. Na, N.; Chang, K.A.; Huang, Z.C.; Lim, H.J. Turbulent flow field and air entrainment in laboratory plunging breaking waves. *J. Geophys. Res. Oceans* **2016**, *121*, 1–30. [[CrossRef](#)]
15. Nadaoka, K.; Hino, M.; Koyano, Y. Structure of the turbulent flow field under breaking waves in the surf zone. *J. Fluid Mech.* **1989**, *204*, 359–387. [[CrossRef](#)]
16. Kubo, H.; Sunamura, T. Large-scale turbulence to facilitate sediment motion under spilling breakers. In Proceedings of the IV Conference on Coastal Dynamics, Lund, Sweden, 11–15 June 2001; pp. 212–221.
17. Ting, F.C.K.; Nelson, J.R. Laboratory measurements of large-scale near-bed turbulent flow structures under spilling regular waves. *Coast. Eng.* **2011**, *58*, 151–172. [[CrossRef](#)]
18. Christensen, E.D.; Deigaard, R. Large eddy simulation of breaking waves. *Coast. Eng.* **2001**, *42*, 53–86. [[CrossRef](#)]
19. Watanabe, Y.; Saeki, H.; Hosking, R.J. Three-dimensional vortex structures under breaking waves. *J. Fluid Mech.* **2005**, *545*, 291–328. [[CrossRef](#)]
20. Ting, F.C.K.; Reimnitz, J. Volumetric velocity measurements of turbulent coherent structures induced by plunging regular waves. *Coast. Eng.* **2015**, *104*, 93–112. [[CrossRef](#)]

21. LeClaire, P.D.; Ting, F.C.K. Measurements of suspended sediment transport and turbulent coherent structures induced by breaking waves using two-phase volumetric three-component velocimetry. *Coast. Eng.* **2017**, *121*, 56–76. [[CrossRef](#)]
22. Ting, F.C.K.; Beck, D.A. Observation of sediment suspension by breaking-wave-generated vortices using volumetric three-component velocimetry. *Coast. Eng.* **2019**, *151*, 97–120. [[CrossRef](#)]
23. Zhou, Z.; Hsu, T.J.; Cox, D.; Liu, X. Large-eddy simulation of wave-breaking induced turbulent coherent structures and suspended sediment transport on a barred beach. *J. Geophys. Res. Oceans* **2017**, *122*, 207–235. [[CrossRef](#)]
24. Lubin, P.; Glockner, S.; Kimmoun, O.; Branger, H. Numerical study of the hydrodynamics of regular waves breaking over a sloping beach. *Eur. J. Mech. B/Fluids* **2011**, *30*, 552–564. [[CrossRef](#)]
25. Lubin, P.; Kimmoun, O.; Véron, F.; Glockner, S. Discussion on instabilities in breaking waves: Vortices, air-entrainment and droplet generation. *Eur. J. Mech. B/Fluids* **2018**, *73*, 144–156. [[CrossRef](#)]
26. Mukaro, R. Vorticity filaments beneath regular turbulent flow. *J. S. Afr. Inst. Civil. Eng.* **2017**, *59*, 2–10. [[CrossRef](#)]
27. Camussi, R. Coherent structure identification from wavelet analysis of particle image velocimetry data. *Exp. Fluids* **2002**, *32*, 76–87. [[CrossRef](#)]
28. Van der Werf, J.; Ribberink, J.; Kranenburg, W.; Neessen, K.; Boers, M. Contributions to the wave-mean momentum balance in the surf zone. *Coast. Eng.* **2017**, *121*, 212–220. [[CrossRef](#)]
29. Truong, S.H.; Uijttewaai, W.S.J.; Stive, M.J.F. Exchange Processes Induced by Large Horizontal Coherent Structures in Floodplain Vegetated Channels. *Water Resour. Res.* **2019**, *55*, 2014–2032. [[CrossRef](#)]
30. Cox, D.T.; Kobayashi, S. Identification of intense, intermittent coherent motions under shoaling and breaking waves. *J. Geophys. Res.* **2000**, *105*, 14223–14236. [[CrossRef](#)]
31. Melville, W.K.; Veron, F.; White, C.J. The velocity field under breaking waves: Coherent structures and turbulence. *J. Fluid. Mech.* **2002**, *454*, 203–233. [[CrossRef](#)]
32. Svendsen, I.A. Analysis of surf zone turbulence. *J. Geophys. Res.* **1987**, *92*, 5115–5124. [[CrossRef](#)]
33. Nezu, I.; Nakagawa, H. *Turbulence in Open-Channel Flows*; Balkema/CRC Press: Boca Raton, FL, USA, 1993.



© 2019 by the authors. Licensee MDPI, Basel, Switzerland. This article is an open access article distributed under the terms and conditions of the Creative Commons Attribution (CC BY) license (<http://creativecommons.org/licenses/by/4.0/>).